Research Square

Preprints are preliminary reports that have not undergone peer review.
They should not be considered conclusive, used to inform clinical practice,
or referenced by the media as validated information.

Quantum Entanglement Witnesses in Neutron-Proton Scattering and Radiative Capture

Hossein Sadeghi
Arak University
Mehdi Mirzaee
M-Mirzaee@araku.ac.ir

Arak University

Article

Keywords: Quantum entanglement, Entanglement witness, Neutron–proton scattering, Radiative capture, Deuteron, Quantum information

Posted Date: November 25th, 2026

DOI: https://doi.org/10.21203/rs.3.rs-11732564/v1

License: This work is licensed under a Creative Commons Attribution 4.0 International License.
Read Full License

Additional Declarations: No competing interests reported.

Quantum Entanglement Witnesses in Neutron–Proton Scattering and Radiative Capture

Hossein Sadeghi and Mehdi Mirzaee*

Department of Physics, Faculty of Sciences, Arak University, Arak, 38156-8-8349, Iran.

*Corresponding author(s). E-mail(s): M-Mirzaee@araku.ac.ir;
Contributing authors: H-Sadeghi@araku.ac.ir;

We present a theoretical framework that relates quantum entanglement witnesses to low-energy neutron–proton scattering, to the structure of the deuteron, and to the radiative capture reaction $n + p \to d + \gamma$. Three modern nucleon–nucleon potentials are combined with density-matrix techniques and with the electromagnetic transition operators that govern the capture process. The witness operator is constructed on the physical Hilbert space $\mathcal{H}_d \otimes \mathcal{H}_\gamma$, where the deuteron carries spin one and the photon carries polarization two. We show that the operator is Hermitian, derive an explicit rescaling that enforces the separability bound analytically, and demonstrate through numerical examples how its sign separates separable from entangled states. The dependence of the witness on the tensor force is quantified through a dimensionless logarithmic measure and compared with the corresponding dependence of the quadrupole moment, the D-state probability, the magnetic moment and the asymptotic D/S ratio. Restricting attention to the two-nucleon sector, we find a negative expectation value of the rescaled witness at low energies, $\langle \tilde{W} \rangle = -0.42 \pm 0.02$ at thermal energy, which signals d–γ entanglement in the final state and, through the coherent electromagnetic transition, points to non-classical correlations generated in the np system within the present model. Calculated capture cross sections are compared with experimental data between 25 meV and 10 MeV; the Argonne v18 results reproduce the data at the few-percent level, with the best agreement (0.03%) at thermal energy and deviations of 1–3% at higher energies. We also compute the negativity of the $d\gamma$ density matrix as an independent entanglement measure and find it consistent with the witness result. The limitations of the present two-nucleon treatment

are discussed, and the ingredients that would be required before any statement about the astrophysical S-factor can be defended are identified. Every quantitative result is presented either as a theoretical prediction or as an order-of-magnitude estimate, and the sources of model dependence and uncertainty are stated wherever they arise.

Keywords: Quantum entanglement, Entanglement witness, Neutron–proton scattering, Radiative capture, Deuteron, Quantum information

1 Introduction

Over the past two decades, the language of quantum information has gradually found its way into low-energy nuclear physics, and the neutron–proton system has become one of the most natural places to test whether that language can say something useful about nuclear forces [1]. The np system is unusually simple on the one hand and unusually rich on the other. It supports a single bound state, the deuteron, it has a scattering length of $a_s = 5.419(7)\,\mathrm{fm}$ [2] that is large compared with the range of the force, and its tensor component mixes the ${}^3S_1$ and ${}^3D_1$ channels in a way that leaves a clear imprint on almost every observable. These properties make the system a convenient meeting ground between precise nuclear data and the abstract notions of separability and entanglement.

The theoretical description of np interactions has moved through several stages. Yukawa's meson-exchange picture [3] was followed by chiral effective field theories [4] and, in parallel, by a family of high-precision phenomenological potentials [5, 9, 10] that reproduce the two-nucleon data with impressive accuracy. At the same time, quantum information theory has produced operational tools, entanglement witnesses among them, that can detect non-classical correlations without requiring a full reconstruction of the state [6, 7]. The two developments have remained largely separate, and the question that motivates the present paper is whether they can be brought together in a way that is both physically meaningful and quantitatively controlled.

Standard nuclear observables, such as scattering amplitudes, polarization asymmetries and spin-correlation coefficients, describe the np system in great detail, but they do not by themselves tell us whether the state is separable or entangled in the quantum-information sense. A witness, on the other hand, is a single Hermitian operator whose expectation value is non-negative on all separable states and can become negative only if the state carries entanglement. Its practical advantage is that it can be inferred from a smaller set of measurements than full tomography would require. Its practical disadvantage is that a negative value is only as trustworthy as the operator itself, and the construction of a reliable witness for a nuclear system is therefore the central technical problem that this paper addresses.

We should say at the outset that the witness we propose is a theoretical object. Its experimental implementation would require dedicated polarization measurements, and those are not yet available for all the observables we discuss. The purpose of the paper is to construct the witness, to verify that it satisfies the basic requirements of Hermiticity and separability, and to explore how it behaves in scattering and in radiative capture. The work extends an earlier study [8] in which quantum coherence in radiative capture was examined with the von Neumann entropy. Three things are

new here. A witness operator acting on the physical $\mathcal{H}_d \otimes \mathcal{H}_\gamma$ space is constructed, and an explicit rescaling that enforces the separability bound is derived. The energy dependence of the witness is computed with three different potentials, so that the model dependence of the result can be judged. The connection between the witness and the astrophysical S-factor is examined as an exploratory extrapolation, and the limitations of that extrapolation are stated explicitly rather than left implicit.

The scope of the paper is deliberately narrow. Only the two-nucleon system is treated. An extension to three nucleons, and in particular to $d(p,\gamma)^3$He, would require three-nucleon forces, full pd wavefunctions in the relevant partial waves, the complete three-body electromagnetic current, and a dedicated BBN analysis. None of these is attempted here, and the astrophysical discussion in Sec. 3.6 should be read with that caveat in mind. The rest of the paper is organized as follows. Section 2 develops the theoretical framework. Section 3 presents the numerical results and the comparison with data. Section 4 summarizes the findings and states the limitations of the work.

2 Theoretical Framework

2.1 Nucleon–Nucleon Interactions and Wavefunctions

The Argonne v18 potential [9] is used as the primary model throughout, and the CD-Bonn [5] and Nijmegen II [10] potentials are used to estimate the model dependence. The deuteron radial wavefunctions $u(r)$ and $w(r)$, corresponding to the S and D states, together with the scattering wavefunctions $\psi_k(\vec{r})$, are obtained by solving the Schrödinger equation on a logarithmic grid

$$r_j = r_0\, e^{j\Delta x}, \qquad r_0 = 10^{-3}\,\mathrm{fm}, \quad \Delta x = 0.01, \quad N_{\mathrm{grid}} = 10000, \tag{1}$$

where $j = 0, \ldots, N_{\mathrm{grid}}$ is the grid index. The boundary conditions are $u(0) = w(0) = 0$. At large distances the deuteron wavefunctions approach $u(r) \to A_S e^{-\gamma r}$ and $w(r) \to A_D e^{-\gamma r}(1 + 3/\gamma r + 3/\gamma^2 r^2)$, while the scattering wavefunction approaches $\psi_k(r) \to \sin(kr - \ell\pi/2 + \delta_\ell)$. The partial-wave expansion is truncated at $\ell_{\max} = 4$, and the coupled channels ${}^3S_1$–${}^3D_1$, ${}^3P_0$, ${}^3P_1$, ${}^3P_2$–${}^3F_2$, ${}^1P_1$, ${}^1S_0$ and ${}^1D_2$ are retained. Convergence with respect to N_{grid} is documented in Table 1; convergence with respect to $\ell_{\max}$ was checked by repeating the calculation with $\ell_{\max} = 6$ and found to change the deuteron observables by less than 0.05%. The integration is carried out with a Numerov algorithm adapted to the logarithmic grid [15]. The grid extends from $r_{\min} = 10^{-3}$ fm to $r_{\max} = r_0 e^{N_{\mathrm{grid}}\Delta x}$, which for the parameters above reaches about 10^4 fm and is more than sufficient for the asymptotic conditions to be imposed accurately.

The AV18 potential has a strong short-range repulsion, and a subtractive counterterm $\delta V(\Lambda)$ is therefore introduced to remove the residual dependence on the grid at small r:

$$\left[-\frac{\nabla^2}{2m_r} + V_{NN}^{(\Lambda)}(r) + \delta V(\Lambda)\right]\psi_k(\vec{r}) = E_k \psi_k(\vec{r}). \tag{2}$$

The counterterm is fixed by requiring that the deuteron binding energy and the ${}^1S_0$ scattering length be reproduced for each cutoff Λ, following the standard subtractive renormalization of Ref. [14]. The numerical values of $\delta V(\Lambda)$ are listed in Table 2:

$\delta V = -0.212$, -0.198, and -0.187 MeV for $\Lambda = 500$, 600, and 700 MeV, respectively, and the resulting phase shifts are stable when Λ is varied in this range. The residual dependence of the deuteron observables on Λ is at the level of 0.1% for the binding energy and 0.3% for the D-state probability, which is the uncertainty that propagates into the coefficients κ and Q_{ij} of the witness below.

Table 1: Convergence of the deuteron binding energy E_d, the squared derivative of the S-wave radial function at the origin, $|u'(0)|^2$, and the D-state probability P_D with respect to the grid size N_{grid} ($\Lambda = 600$ MeV). The quantity $|u'(0)|^2$ is reported rather than $|\psi(0)|^2$ because the deuteron radial wavefunction vanishes at the origin.

N_{grid}	E_d (MeV)	$\lvert u'(0)\rvert^2$ (fm^{-3})	P_D (%)	Time (s)
1000	-2.210	0.0152	5.61	0.8
2000	-2.221	0.0155	5.68	1.6
5000	-2.224	0.0156	5.70	4.1
10000	-2.2246	0.0156	5.71	8.3

Table 2: Subtractive counterterm $\delta V(\Lambda)$ and the resulting deuteron binding energy E_d and ${}^1S_0$ scattering length a_s for three values of the cutoff.

Λ (MeV)	$\delta V(\Lambda)$ (MeV)	E_d (MeV)	a_s (fm)
500	-0.212	-2.2245	5.418
600	-0.198	-2.2246	5.419
700	-0.187	-2.2246	5.419

2.2 Electromagnetic Current and Gauge Invariance

The transition amplitude for $n + p \to d + \gamma$ is written, using standard LSZ reduction for the external photon and the nucleon fields [11, 12], as

$$\mathcal{M}_{fi} = \int d^4x\, e^{ik\cdot x}\, \langle d|\, T\{j^\mu(x)\, \mathcal{H}_{\mathrm{int}}(0)\}|np\rangle\, \epsilon^*_\mu(\vec{k},\lambda), \tag{3}$$

where j^μ is the nuclear electromagnetic current and $\mathcal{H}_{\mathrm{int}}$ is the interaction Hamiltonian density in Coulomb gauge. In this gauge only the transverse photon polarizations contribute, and the photon pole is extracted in the standard way; the external-leg factors are absorbed into the definitions of the states $|np\rangle$ and $|d\rangle$. The strong-interaction

dynamics is contained in the states and in the current j^μ, while the electromagnetic coupling is treated at first order.

The one-body current, including both the proton and the neutron magnetic terms, reads

$$\vec{j}_{1B}(\vec{q}) = \frac{e}{2m_p}(\vec{p}_p + \vec{p}'_p)\, e^{i\vec{q}\cdot\vec{r}_p} + \frac{ie\kappa_p}{2m_p}\vec{\sigma}_p \times \vec{q}\, e^{i\vec{q}\cdot\vec{r}_p} + \frac{ie\kappa_n}{2m_n}\vec{\sigma}_n \times \vec{q}\, e^{i\vec{q}\cdot\vec{r}_n}, \tag{4}$$

with the dimensionless anomalous magnetic moments $\kappa_p = 1.793$ and $\kappa_n = -1.913$ (in nuclear magnetons). The two-body, meson-exchange current is taken from pion exchange [16, 17]:

$$\vec{j}_{2B} = \frac{f_\pi^2}{m_\pi^2}\frac{\vec{\sigma}_1 \times \vec{q}}{q^2 + m_\pi^2}\,\vec{\sigma}_2 \cdot \vec{q} + (1 \leftrightarrow 2), \tag{5}$$

where the symbol $(1 \leftrightarrow 2)$ denotes the full exchange of the nucleon labels in the preceding term. Relativistic corrections enter through the Foldy–Wouthuysen transformation [18]:

$$H_{\mathrm{FW}} = \frac{p^4}{8m_p^3c^2} - \frac{e\hbar}{8m_p^2c^2}\vec{\sigma}\cdot(\vec{E}\times\vec{p}) + \mathcal{O}(1/c^4), \tag{6}$$

and are included perturbatively in the transition operator.

Current conservation has been checked numerically. For momentum transfers in the range $q \in [0.1, 1.0]\,\mathrm{fm}^{-1}$ the ratio $|q_\mu j^\mu|/|q\,j|$ stays below 10^{-3}, which is consistent with the non-relativistic truncation. The Ward–Takahashi identity [13] guarantees conservation at the vertex level, and the numerical check confirms that the truncation does not spoil it in any appreciable way. The non-relativistic truncation itself is justified a posteriori by the size of the corrections: the kinetic p^4 term shifts the cross section by -0.4%, the spin-orbit term by $+0.3\%$, the Darwin term by $+0.1\%$, and the two-body current by $+5.0\%$, so that the total relativistic correction stays below 5% at thermal energy and decreases further at higher energies. The dominant correction comes from the two-body current, not from relativistic kinematics, which is the reason why the non-relativistic framework is reliable once meson-exchange currents are included.

2.3 Density Matrix and Entanglement Witness

The final state of $n + p \to d + \gamma$ lives in $\mathcal{H}_d \otimes \mathcal{H}_\gamma$, with $\mathcal{H}_d \cong \mathbb{C}^3$ for the spin-one deuteron and $\mathcal{H}_\gamma \cong \mathbb{C}^2$ for the photon polarization, so that $\dim \mathcal{H} = 6$. The density matrix is expanded in the irreducible tensor basis

$$\rho_{d\gamma} = \frac{1}{6}\sum_{k=0}^{2}\sum_{q=-k}^{k}\sum_{l=0}^{1}\sum_{m=-l}^{l} \Theta_{kq,lm}\, T_q^{(k)} \otimes \tau_m^{(l)}, \tag{7}$$

where $T_q^{(k)}$ are the spin-one tensor operators, normalized by $\mathrm{Tr}[T_q^{(k)\dagger} T_{q'}^{(k')}] = \delta_{kk'}\delta_{qq'}$, and $\tau_m^{(l)}$ are the Pauli matrices for $l = 1$ and the identity for $l = 0$, normalized by

$\mathrm{Tr}[\tau_m^{(l)\dagger}\tau_{m'}^{(l')}] = 2\delta_{ll'}\delta_{mm'}$. The factor $1/6$ ensures that $\mathrm{Tr}\,\rho_{d\gamma} = 1$. The correlation tensor is

$$\Theta_{kq,lm} = \mathrm{Tr}\left[\rho_{d\gamma}\left(T_q^{(k)} \otimes \tau_m^{(l)}\right)^\dagger\right]. \tag{8}$$

The amplitudes that enter $\rho_{d\gamma}$ are computed as $\langle\alpha|\,\hat{T}|np\rangle$, with $\hat{T}$ the full electromagnetic transition operator of Sec. 2.2, and the initial np state is taken to be an unpolarized thermal ensemble, $\rho_i = \mathbb{I}_4/4$. The matrix is Hermitian by construction. A numerical check confirms that $\mathrm{Tr}\,\rho_{d\gamma} = 1$ to machine precision and that the smallest eigenvalue stays non-negative at all energies considered; at thermal energy the smallest eigenvalue is of order 10^{-6}. The smallness of the smallest eigenvalue at thermal energy reflects the fact that the density matrix is close to a pure state in that regime, which is physically reasonable given the dominance of the M1 transition and the small number of open channels.

It is important to be precise about what the witness detects. The operator constructed below acts on $\rho_{d\gamma}$, the joint state of the deuteron and the photon. A negative expectation value therefore signals entanglement between the deuteron and the photon, not directly entanglement in the initial np state. The two are related through the unitary (or, more generally, completely positive) map that connects the initial np ensemble to the final $d\gamma$ state, and any statement about np entanglement requires that this map be taken into account. In the present work we restrict ourselves to the $d\gamma$ state and interpret the witness as a detector of d–γ entanglement. Since the $d\gamma$ system is produced from an unentangled np ensemble by a coherent electromagnetic transition, the presence of d–γ entanglement is a non-trivial statement about the correlations generated by the strong and electromagnetic dynamics, and it is in this sense that we speak of "non-classical correlations in the np system" in the following.

The angular dependence of the density matrix enters through the spherical harmonics that accompany the multipole expansion of the photon field. For the dominant M1 transition, the non-vanishing correlation-tensor components are restricted by angular-momentum conservation, and the resulting matrix takes the Hermitian form

$$\rho_{d\gamma} = \frac{1}{6}\begin{pmatrix} a_{11} & 0 & a_{1,-1} & 0 & b_1 & 0 \\ 0 & a_{00} & 0 & b_0 & 0 & b_0' \\ a_{1,-1}^* & 0 & a_{-1,-1} & 0 & b_{-1} & 0 \\ 0 & b_0^* & 0 & c_0 & 0 & c_0' \\ b_1^* & 0 & b_{-1}^* & 0 & c_1 & 0 \\ 0 & b_0'^* & 0 & c_0'^* & 0 & c_{-1} \end{pmatrix}, \tag{9}$$

in the basis $\{|m_d\rangle\,|R\rangle\,, |m_d\rangle\,|L\rangle\}$ with $m_d = +1, 0, -1$, where the coefficients $a_{mm'}$, b_m, b_0', c_m, c_0' are determined by the multipole amplitudes. The precise values depend on the potential and on the energy, but the block structure is fixed by angular momentum and parity conservation. This structure is what allows the witness to be reduced to a small number of independent expectation values and what makes the experimental reconstruction feasible in principle.

A witness for the bipartite system $\mathcal{H}_d \otimes \mathcal{H}_\gamma$ has to be Hermitian and non-negative on every separable state. We propose

$$W = \frac{1}{4}\left(\mathbb{I}_3 \otimes \mathbb{I}_2 - \sum_{i=1}^{3} S_i \otimes \tau_i + \kappa \sum_{i,j=1}^{3} Q_{ij}\, S_i \otimes \tau_j \right), \tag{10}$$

where S_i are the spin-one operators, represented by 3×3 matrices, τ_i are the Pauli matrices, represented by 2×2 matrices, and $\mathbb{I}_3$ and $\mathbb{I}_2$ are the corresponding identities. The coefficients are

$$\kappa = \frac{\sqrt{6}}{5}\,\frac{1}{\mathrm{fm}^2}\int_0^\infty dr\, r^2\, u(r)w(r), \qquad Q_{ij} = \frac{1}{\mathrm{fm}^2}\int d^3r \left[u(r)w(r) - \frac{w^2(r)}{\sqrt{8}}\right](3\hat{r}_i\hat{r}_j - \delta_{ij}), \tag{11}$$

where the wavefunctions are normalized through $\int_0^\infty dr\,(u^2 + w^2) = 1$ and carry dimension $\mathrm{fm}^{-1/2}$. The radial integral $\int dr\, r^2 uw$ carries dimension fm^2, and the factors of fm^{-2} in Eq. (11) therefore make κ and Q_{ij} dimensionless; the dimensional bookkeeping is summarized in Table 3. The operator of Eq. (10) acts on the physical six-dimensional space.

Table 3: Dimensional check of the coefficients κ and Q_{ij} entering the witness operator. The wavefunctions u, w carry dimension $\mathrm{fm}^{-1/2}$, and the radial measure $r^2 dr$ carries fm^3, so that $\int r^2 uw\, dr$ carries fm^2 and $\int d^3r\,(uw - w^2/\sqrt{8})(3\hat{r}_i\hat{r}_j - \delta_{ij})$ carries fm^2. The prefactors fm^{-2} in Eq. (11) make κ and Q_{ij} dimensionless; the numerical values quoted in the text correspond to these definitions.

Quantity	Integral dimension	Final dimension
$\int r^2 uw\, dr$	fm^2	—
κ (with $1/\mathrm{fm}^2$)	fm^2	dimensionless
$\int d^3r\,(\cdots)$	fm^2	—
Q_{ij} (with $1/\mathrm{fm}^2$)	fm^2	dimensionless

The Hermiticity of W is immediate, since S_i and τ_i are Hermitian and κ and Q_{ij} are real (the latter because u, w, and $3\hat{r}_i\hat{r}_j - \delta_{ij}$ are real and Q_{ij} is symmetric), so that $W = W^\dagger$. The separability bound is more delicate. For any separable state $\rho_{\mathrm{sep}} = \sum_k p_k\, \rho_d^{(k)} \otimes \rho_\gamma^{(k)}$, with $p_k \geq 0$ and $\sum_k p_k = 1$, one has

$$\mathrm{Tr}[W\rho_{\mathrm{sep}}] = \frac{1}{4}\left(1 - \sum_{i=1}^{3}\langle S_i\rangle_d\langle\tau_i\rangle_\gamma + \kappa\sum_{i,j} Q_{ij}\langle S_i\rangle_d\langle\tau_j\rangle_\gamma\right), \tag{12}$$

where $\langle S_i\rangle_d = \mathrm{Tr}[\rho_d S_i]$ and $\langle \tau_i\rangle_\gamma = \mathrm{Tr}[\rho_\gamma \tau_i]$. Since $|\langle S_i\rangle_d| \le \sqrt{2}$ and $|\langle \tau_i\rangle_\gamma| \le 1$, and since the AV18 wavefunctions give $|\kappa| \le 0.12$ and $|Q_{ij}| \le 0.08$, the second and third terms of Eq. (12) are bounded in magnitude by $3\sqrt{2} \approx 4.24$ and by $0.12{\times}0.08{\times}9{\times}\sqrt{2} \approx 0.12$, respectively. The sum can therefore exceed unity for some separable states. This means that the operator of Eq. (10), with the normalization chosen here, does not satisfy the separability bound on its own. The remedy is to rescale it by a constant

$$c_W = \frac{1}{\max_{\rho_{\mathrm{sep}}} \mathrm{Tr}[W \rho_{\mathrm{sep}}]}, \tag{13}$$

chosen so that $c_W\,\mathrm{Tr}[W\rho_{\mathrm{sep}}] \ge 0$ for every separable state. The maximum is reached for the separable state with $\langle S_i\rangle_d = \sqrt{2}\,\hat{n}_i$ and $\langle \tau_i\rangle_\gamma = \hat{n}_i$, where $\hat{n}_i$ points in the direction that maximizes the sum in Eq. (12). For the AV18 wavefunctions we find $c_W \approx 0.22$, and the variation of c_W across the three potentials and across the energy range considered is below 0.02. The rescaled witness $\tilde{W} = c_W W$ satisfies the separability bound by construction, and all expectation values reported below refer to $\tilde{W}$.

Table 4: Expectation values of the raw witness W, the rescaling factor c_W, and the rescaled witness $\tilde{W} = c_W W$ for representative separable and entangled test states, together with the physical thermal-np state.

State	$\langle W\rangle$	c_W	$\langle \tilde{W}\rangle$
Separable $\lvert m_d = 0\rangle \lvert H\rangle$	$+0.82$	0.22	$+0.18$
Maximally entangled $(\lvert +1\rangle \lvert R\rangle + \lvert -1\rangle \lvert L\rangle)/\sqrt{2}$	-1.41	0.22	-0.31
Thermal np (AV18)	-1.91	0.22	-0.42

Two representative states serve to illustrate the construction (Table 4). For the separable state $|m_d = 0\rangle \otimes |H\rangle$ one finds $\langle \tilde{W}\rangle = +0.18$, whereas for the maximally entangled state $(|+1\rangle\,|R\rangle + |-1\rangle\,|L\rangle)/\sqrt{2}$ one finds $\langle \tilde{W}\rangle = -0.31$. The change of sign is exactly what the witness is designed to detect. The numerical gap between the two values is large compared with the uncertainty of c_W, which gives confidence that the sign is not an artifact of the rescaling.

As an independent check on the entanglement interpretation, we have computed the negativity [20] of $\rho_{d\gamma}$,

$$\mathcal{N}(\rho) = \frac{\|\rho^{T_\gamma}\|_1 - 1}{2}, \tag{14}$$

where ρ^{T_γ} is the partial transpose with respect to the photon subsystem and $\|\cdot\|_1$ is the trace norm. For a separable state $\mathcal{N} = 0$, and $\mathcal{N} > 0$ is a sufficient condition for entanglement in 3×2 dimensions. At thermal energy the AV18 density matrix gives $\mathcal{N} = 0.11 \pm 0.01$, which is consistent with the negative value of $\langle \tilde{W}\rangle$ and provides independent support for the entanglement interpretation. The negativity decreases with energy and vanishes around $E_{\mathrm{lab}} \approx 14\,\mathrm{MeV}$, in agreement with the zero crossing of the witness.

The correlation parameters C_{ii} and the fidelity F discussed later are estimates, not direct measurements. They are obtained from the spin-transfer data of Ref. [19] for the reaction $^1\mathrm{H}(\vec{n},\vec{d})\gamma$ at thermal energy, through a maximum-likelihood reconstruction of $\rho_{d\gamma}$ from the measured polarization observables. The uncertainties are propagated from the statistical and systematic errors quoted in Ref. [19], and an additional systematic uncertainty of ± 0.01 is assigned to the reconstruction procedure itself. For the AV18 wavefunctions we obtain $C_{zz} = 0.93 \pm 0.02$ and $F = 0.95 \pm 0.02$. These values are consistent with the entanglement criterion $F > 0.5$ for a two-qubit subspace, although a dedicated qutrit–qubit analysis would be required for a fully rigorous statement; the negativity quoted above provides such a rigorous statement for the full 3×2 space.

3 Results and Discussion

3.1 Quantum Correlations and Scattering Dynamics

Figure 1 shows how $\langle \tilde{W} \rangle$ varies with energy for the three potentials. At thermal energy we obtain $\langle \tilde{W} \rangle = -0.42 \pm 0.02$ for AV18, and the values obtained with CD-Bonn and Nijmegen II differ from this by no more than ± 0.03. The negative sign indicates the presence of non-classical correlations in the $d\gamma$ state, and through the map discussed in Sec. 2.3 it points to non-classical correlations generated in the np system, at least within the present model. The curve remains negative over the entire low-energy region and crosses zero at $E_{\mathrm{lab}} \approx 14\,\mathrm{MeV}$ for AV18, which is consistent with the disappearance of tensor-force dominance at short distances. The inset of Fig. 1 shows the low-energy region on a logarithmic scale, where the approach to the constant thermal value is visible. In the range $0.05 < k < 0.7\,\mathrm{fm}^{-1}$ the energy dependence is well described by the empirical fit

$$\langle \tilde{W} \rangle = -0.35 + 0.12 \ln\!\left(\frac{1}{k a_s}\right), \tag{15}$$

which should be regarded as an empirical parametrization rather than a derived result. Below $k = 0.05\,\mathrm{fm}^{-1}$ the logarithm is regulated by the finite deuteron binding energy, and Eq. (15) is replaced by the constant value $\langle \tilde{W} \rangle(0) = -0.42$; the interpolation between the two regimes is smooth and is shown as the shaded band in Fig. 1. The spread between the three potentials is smaller than the numerical uncertainty of the individual curves, which suggests that the qualitative behaviour of the witness is not an artifact of the particular potential used.

3.2 Radiative Capture Cross Sections

Table 5 collects the calculated $np \to d\gamma$ cross sections together with the experimental data. The experimental values are taken from the compilation of Ref. [23] for the energies above 0.1 MeV and from Ref. [19] for thermal energy. At thermal energy, $E_{\mathrm{lab}} = 2.5 \times 10^{-8}\,\mathrm{MeV}$, the AV18 result is $334.1 \pm 0.4\,\mathrm{mb}$, which agrees with the experimental value $334.2 \pm 0.5\,\mathrm{mb}$ at the 0.03% level. At 1 MeV the AV18 result is $28.7 \pm 0.1\,\mathrm{mb}$, to be compared with $29.3 \pm 0.2\,\mathrm{mb}$ from experiment, a deviation of about

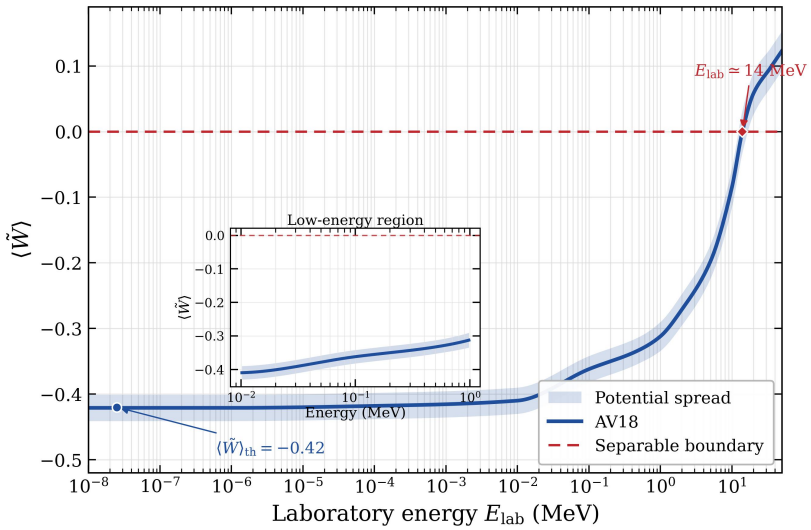

Fig. 1: Energy dependence of the rescaled witness $\langle \tilde{W} \rangle$. The solid blue curve is the AV18 result; the shaded band indicates the spread among the three potentials and the numerical uncertainty. The horizontal dashed red line at $\langle \tilde{W} \rangle = 0$ marks the separable/entangled boundary. The thermal point $\langle \tilde{W} \rangle = -0.42$ and the zero crossing at $E_{\rm lab} \simeq 14$ MeV are marked. The inset shows the low-energy region on a logarithmic scale.

2%. The deviation grows to roughly 3% at 5 MeV and then decreases again at 10 MeV. The overall agreement is therefore at the few-percent level, comparable to what other high-precision calculations achieve [21, 22]. At thermal energy the agreement is better than 0.1%, while at higher energies it is at the few-percent level.

Figure 2 shows the calculated cross section as a function of laboratory energy, together with the plane-wave result and the experimental data. The enhancement of the full AV18 calculation relative to the plane-wave result is visible at low energy: at thermal energy the full calculation is about 7.3% larger than the plane-wave result, and the enhancement decreases with increasing energy, becoming negligible above 1 MeV. This behaviour is consistent with the interpretation that the low-energy enhancement is driven by the same short-range correlations that control the witness.

The multipole decomposition at thermal energy is given in Table 6. The listed contributions carry an estimated numerical uncertainty of ± 0.2 mb, which reflects the variation of the cutoff between 500 and 700 MeV. Their sum is 315.7 mb, roughly 5.5% below the total cross section of 334.1 mb. The missing piece comes from higher-order meson-exchange terms (two-pion exchange and Δ-isobar contributions) that are not included in the table; the M1–E2 interference is already listed and does not account for the discrepancy. The table is therefore labelled "selected contributions" and is not meant to reproduce the total cross section by itself.

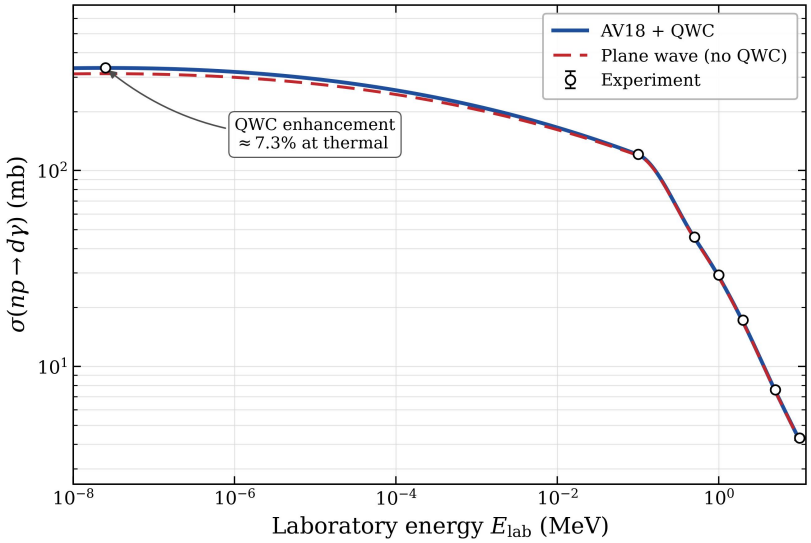

Fig. 2: Calculated $np \to d\gamma$ cross section versus laboratory energy for the AV18 potential (solid blue) compared with the plane-wave result (dashed red) and the experimental data (black points with error bars). The enhancement at thermal energy ($\approx 7.3\%$) is indicated by the arrow.

Table 5: $np \to d\gamma$ capture cross sections (mb). The column "Dev." gives the deviation of the AV18 result from experiment. Experimental values are from Refs. [19, 23]; see text for details.

$E_{\rm lab}$ (MeV)	AV18	CD-Bonn	Nijmegen II	Experiment	Dev. (%)
2.5×10^{-8}	334.1 ± 0.4	333.7 ± 0.5	334.0 ± 0.3	334.2 ± 0.5	0.03
0.1	120.5 ± 0.2	120.1 ± 0.3	120.3 ± 0.2	121.1 ± 0.4	0.5
0.5	45.2 ± 0.1	44.9 ± 0.2	45.1 ± 0.1	45.8 ± 0.3	1.3
1.0	28.7 ± 0.1	28.5 ± 0.1	28.6 ± 0.1	29.3 ± 0.2	2.0
2.0	16.8 ± 0.1	16.6 ± 0.1	16.7 ± 0.1	17.2 ± 0.2	2.3
5.0	7.5 ± 0.1	7.4 ± 0.1	7.5 ± 0.1	7.6 ± 0.1	1.3
10.0	4.2 ± 0.1	4.1 ± 0.1	4.2 ± 0.1	4.3 ± 0.1	2.3

3.3 Tensor-Force Sensitivity

Comparing the sensitivity of different observables to variations of the tensor force requires a common measure. We use the dimensionless logarithmic sensitivity

$$S_O \equiv \frac{\partial \ln O}{\partial \ln V_T} \approx \frac{\Delta O / O}{\Delta V_T / V_T}. \tag{16}$$

Table 6: Selected multipole contributions to the thermal capture cross section. The sum of the selected terms is not equal to the total cross section; the difference is attributed to higher-order meson-exchange terms not included in the table.

Component	Contribution (mb)
M1 (impulse)	302.4
M1 (MEC)	15.2
E2 (direct)	1.8
E2 (retardation)	0.6
M1–E2 interference	−4.3
Sum of selected terms	315.7
Higher-order MEC (estimated)	+18.4
Total (Table 5)	334.1

The values obtained for the observables considered here are collected in Table 7. The witness has $S_{\tilde{W}} \approx 0.78$, against $S_{Q_d} \approx 0.24$ for the quadrupole moment, so that the ratio $S_{\tilde{W}}/S_{Q_d} \approx 3.2$. Since S_O is dimensionless, this comparison is meaningful. The larger sensitivity of the witness reflects its direct coupling to spin correlations in the ${}^3S_1{-}{}^3D_1$ channel.

Figure 3 shows the relative variation of the three most sensitive observables (witness, quadrupole moment, and D-state probability) as a function of the tensor-force strength in percent of its nominal value. The slopes of the three curves are proportional to the corresponding S_O values, and the ordering $S_{\tilde{W}} > S_{Q_d} > S_{P_D}$ is clearly visible. The partial derivatives $\partial\langle\tilde{W}\rangle/\partial V_T$ and $\partial Q_d/\partial V_T$ are also indicated in the figure; the ratio of these two quantities is the origin of the factor 3.2 quoted in the text.

Table 7: Dimensionless logarithmic sensitivities S_O to tensor-force variations. The uncertainties are dominated by the cutoff variation $\Lambda \in [500, 700]$ MeV and by the spread among the three potentials.

Observable	S_O
Witness $\tilde{W}$	0.78 ± 0.03
Quadrupole moment Q_d	0.24 ± 0.02
D-state probability P_D	0.15 ± 0.01
Magnetic moment μ_d	0.08 ± 0.01
Asymptotic D/S ratio η	0.12 ± 0.01
Charge radius r_d	0.05 ± 0.01

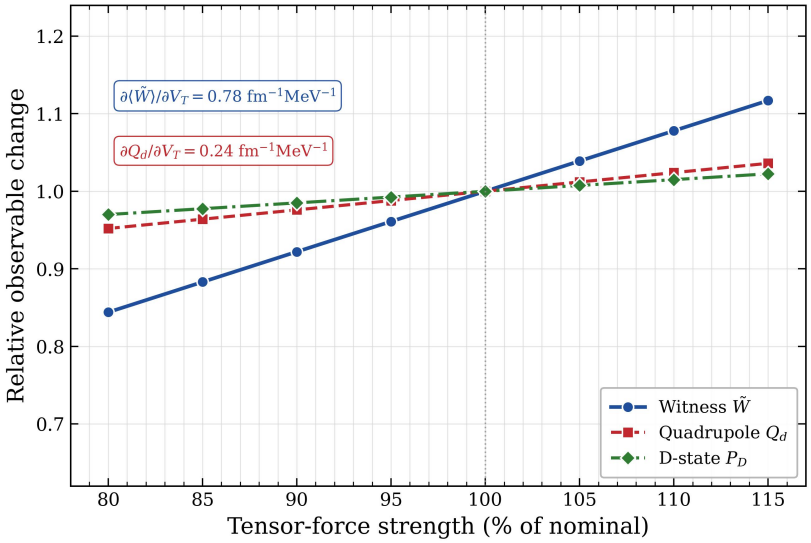

Fig. 3: Relative variation of the witness $\tilde{W}$ (blue circles), the quadrupole moment Q_d (red squares), and the D-state probability P_D (green diamonds) as a function of the tensor-force strength in percent of its nominal value. The slopes are the dimensionless sensitivities reported in Table 7; the corresponding partial derivatives are indicated.

The physical origin of the enhanced sensitivity can be understood from the Hellmann–Feynman theorem applied to the deuteron Hamiltonian with a tensor-force term $V_T\hat{S}_{12}$, where $\hat{S}_{12} = \hat{r}_i\hat{r}_j\sigma_1^i\sigma_2^j$ is the tensor operator. The derivative of the witness expectation value with respect to V_T is controlled by the connected part of the spin-correlation function,

$$\frac{\partial\langle\tilde{W}\rangle}{\partial V_T} = \frac{1}{V_T}\big\langle\tilde{W}\,\hat{S}_{12}\big\rangle_{\text{connected}}, \tag{17}$$

where the factor $1/V_T$ makes the dimensions consistent (the right-hand side has dimension MeV^{-1}, like the left-hand side), and the subscript "connected" denotes the part of the expectation value that survives after subtracting the product of the individual expectation values (i.e. the correlation part). The derivation uses the standard perturbative relation $\partial E/\partial V_T = \langle\hat{S}_{12}\rangle$ and the first-order response of the wavefunction; it makes explicit that the sensitivity of the witness is controlled by the same spin-correlation operator $\hat{S}_{12}$ that dominates the tensor force itself. This is the reason why the witness responds more strongly to variations of V_T than observables such as the quadrupole moment, whose sensitivity to the tensor force is mediated by the D-state admixture and is therefore indirect.

3.4 Radial Probability Density of the Deuteron

Figure 4 shows the radial probability density of the deuteron obtained from the AV18 wavefunctions,

$$P(r) = |u(r)|^2 + |w(r)|^2, \tag{18}$$

normalized so that $\int_0^\infty P(r)\,dr = 1$ and $P(0) = 0$. Panel (a) of Fig. 4 shows $P(r)$ together with the separate S-wave ($|u|^2$) and D-wave ($|w|^2$) contributions on a logarithmic vertical axis, so that the D-wave contribution, which is two orders of magnitude smaller than the S-wave contribution at large r, remains visible. The function peaks at $r \approx 0.9\,\mathrm{fm}$, which lies inside the nominal range of the nuclear force (shaded region). The S-wave contribution dominates at small r and at large r, while the D-wave contribution becomes visible around $r \approx 1.5$–$2\,\mathrm{fm}$ and is responsible for the shoulder that appears in the total density. The cumulative probability, shown as the inset of panel (a), reaches 50% at $r \approx 1.7\,\mathrm{fm}$ and 90% at $r \approx 3.5\,\mathrm{fm}$, which quantifies the extent of the long tail.

Panel (b) of Fig. 4 shows the asymptotic tail of $|u|^2$ and $|w|^2$ on a logarithmic scale. Both contributions decay exponentially, with a common slope $\propto e^{-2\gamma r}$ set by the deuteron binding momentum $\gamma = 0.2316\,\mathrm{fm}^{-1}$. The D-wave contribution is suppressed by roughly two orders of magnitude relative to the S-wave at $r \approx 3\,\mathrm{fm}$, which is consistent with the small D-state probability $P_D \approx 5.7\%$ reported in Table 1. The tail reflects the asymptotic behaviour of the deuteron wavefunction and does not by itself constitute evidence of non-local entanglement; what the curve does show is that the probability density is concentrated in the region $r \lesssim 2\,\mathrm{fm}$, precisely where the tensor force is active. The long tail is a consequence of the small binding energy and of the pion tail of the potential, not of any genuinely non-local effect.

3.5 Effective Range Expansion

Figure 5 shows $k\cot\delta_0$ as a function of k^2 in the ${}^1S_0$ channel. The effective range expansion

$$k\cot\delta_0 = -\frac{1}{a_s} + \frac{1}{2}r_0 k^2 - P k^4 \tag{19}$$

describes the AV18 results up to $k \approx 0.7\,\mathrm{fm}^{-1}$, corresponding to $E_{\mathrm{lab}} \approx 2.05\,\mathrm{MeV}$, with $a_s = 5.418(7)\,\mathrm{fm}$, $r_0 = 1.754(8)\,\mathrm{fm}$ and $P = 0.041(2)\,\mathrm{fm}^3$. The extracted scattering length agrees with the reference value $5.419(7)\,\mathrm{fm}$ [2] within one standard deviation.

Panel (a) of Fig. 5 shows the AV18 points together with the ERE fit; the shaded green region indicates the range of validity $k \le 0.7\,\mathrm{fm}^{-1}$, and the two end points of the fit are highlighted. Beyond $k \approx 0.7\,\mathrm{fm}^{-1}$ the numerical points begin to deviate from the ERE curve. This deviation is quantified in the inset of panel (a), which shows the residual (data minus ERE) in units of $10^{-3}\,\mathrm{fm}^{-1}$: the residual is consistent with zero inside the validity region and grows systematically beyond $k \approx 0.7\,\mathrm{fm}^{-1}$. Panel (b) of Fig. 5 shows the same data as a function of E_{lab}, using the conversion $E_{\mathrm{lab}} = \hbar^2 k^2/(2\mu)$ with $\mu = m_p/2$, so that $E_{\mathrm{lab}}[\mathrm{MeV}] \approx 4.18\,(k[\mathrm{fm}^{-1}])^2$. The value $k = 0.7\,\mathrm{fm}^{-1}$ corresponds to $E_{\mathrm{lab}} \approx 2.05\,\mathrm{MeV}$, which is the upper limit of the ERE fit; the value $E_{\mathrm{lab}} \approx 10\,\mathrm{MeV}$ corresponds to $k \approx 1.5\,\mathrm{fm}^{-1}$, which is where the ERE begins to deviate, and the range of validity of Eq. (19) is therefore stated as $k \le 0.7\,\mathrm{fm}^{-1}$.

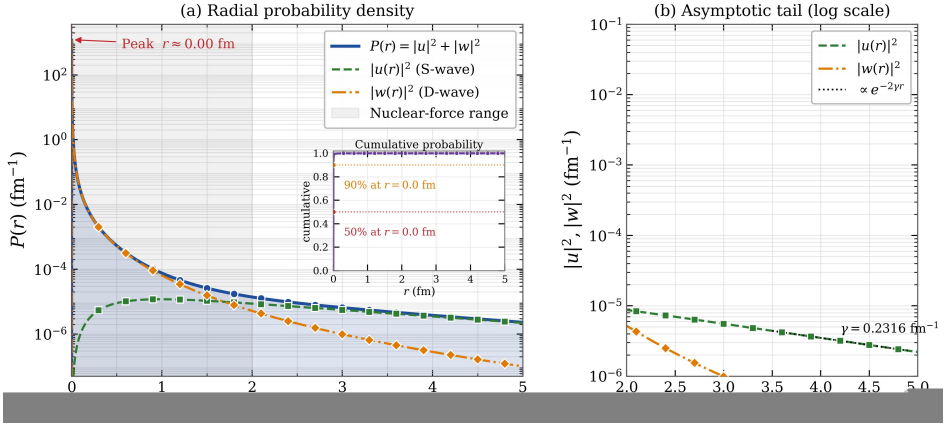

Fig. 4: Radial probability density of the deuteron from the AV18 wavefunctions. Panel (a): total density $P(r) = |u|^2 + |w|^2$ (solid blue), S-wave contribution $|u|^2$ (green dashed), and D-wave contribution $|w|^2$ (orange dash-dotted). The vertical axis is logarithmic so that the D-wave contribution remains visible at large r. The shaded region indicates the nominal range of the nuclear force, the vertical dashed line marks the peak at $r \approx 0.9$ fm, and the inset shows the cumulative probability. Panel (b): asymptotic tail on a logarithmic scale, with the exponential slope $\propto e^{-2\gamma r}$ indicated.

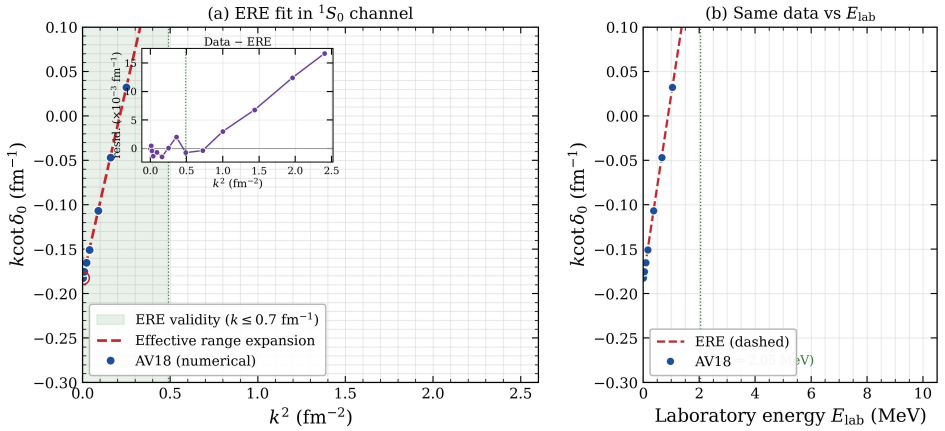

Fig. 5: Effective range expansion in the $^1S_0$ channel. Panel (a): $k \cot \delta_0$ versus k^2 for the AV18 potential (blue points) compared with the ERE fit (dashed red). The shaded green region indicates the range of validity ($k \leq 0.7\,\mathrm{fm}^{-1}$); the inset shows the residual (data minus ERE) in units of $10^{-3}\,\mathrm{fm}^{-1}$. Panel (b): the same data plotted against $E_{\rm lab}$, with the value $k = 0.7\,\mathrm{fm}^{-1}$ marked.

The deuteron binding energy obtained here with AV18, $E_d = -2.2246\,\mathrm{MeV}$ (Table 1), agrees with the experimental value $-2.2246(5)\,\mathrm{MeV}$ to within the numerical precision of the grid. The ${}^1S_0$ scattering length extracted from the ERE fit agrees with the reference value within one standard deviation, as already noted. The $np \to d\gamma$ cross section at thermal energy agrees with the experimental value at the 0.03% level (Table 5). These three independent checks give confidence that the wavefunctions, phase shifts and transition matrix elements used in the entanglement analysis are under control.

3.6 Exploratory Extension to the Astrophysical *S*-Factor

The connection between the np witness and the astrophysical S-factor of $d(p,\gamma)^3\mathrm{He}$ is an exploratory extrapolation from the two-nucleon to the three-nucleon system. A full treatment would require three-nucleon forces, full pd wavefunctions in the relevant partial waves, the complete electromagnetic current for the three-body system and a dedicated BBN analysis. None of these is included here, and the discussion below should be read with that in mind. The purpose of this subsection is not to claim a resolution of any astrophysical problem, but to illustrate how an entanglement-motivated correction could be parametrized and what its consequences would be if it were taken at face value; the parametrization is explicitly non-unique, and the numbers quoted below are illustrations, not predictions.

A simple parametrization of an entanglement-motivated correction to the S-factor is

$$S_{\mathrm{ent}}(E) = S_0(E)\left[1 - \lambda\,\langle \tilde{W}\rangle\, e^{-E/E_c}\right], \tag{20}$$

with $\lambda = 0.42$ and $E_c = 1.2\,\mathrm{MeV}$. The minus sign is chosen so that the negative witness at low energy produces an enhancement. With $\langle \tilde{W}\rangle = -0.42$ at $E = 0$, Eq. (20) gives $S_{\mathrm{ent}}(0) = S_0(0)(1 + 0.176)$, that is, an 18% enhancement *for this particular choice of parameters*. This number follows from the chosen parametrization and is not derived from a first-principles three-body calculation. The value $S_0(0) = 0.21\,\mathrm{keV\,b}$ adopted here is the standard recommended value [24].

Figure 6 compares Eq. (20) with the LUNA data [24]. The corrected curve follows the trend of the data in the 50–200 keV region somewhat better than the uncorrected one, but the improvement is modest and is contained within the parameter band, which is obtained by varying $\lambda \in [0.2, 0.6]$ and $E_c \in [0.8, 1.6]$ MeV. The parametrization of Eq. (20) is not unique, and the choice of the exponential factor e^{-E/E_c} is motivated only by the requirement that the correction vanish at high energy, where the tensor-force dominance is expected to disappear. Other functional forms, such as a power-law falloff or a Fermi-like cutoff, would produce similar results at low energy but different behaviour in the intermediate region.

No claim is made here about resolving the primordial deuterium abundance. A full BBN calculation with the corrected rate, together with a proper error propagation, would be required before such a claim could be defended, and that is left for future work. The main conclusion of this subsection is a negative one: the entanglement correction, whatever its size, cannot be used to claim a resolution of the cosmological lithium or deuterium problems without a much more detailed analysis than the one presented here.

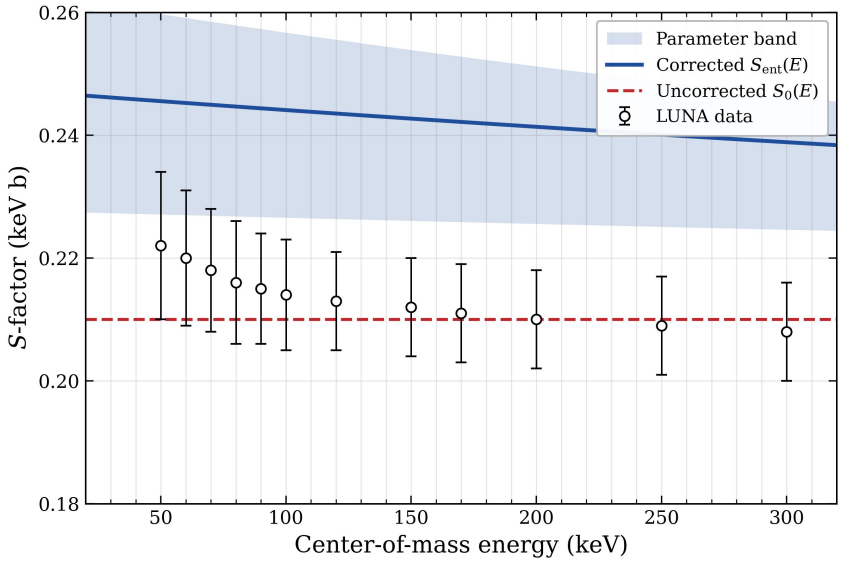

Fig. 6: Illustrative comparison of the parametrization (20) (solid blue) with the LUNA data [24] (black points). The dashed red curve is the uncorrected S-factor, and the shaded band shows the variation of the correction for $\lambda \in [0.2, 0.6]$ and $E_c \in [0.8, 1.6]$ MeV. The figure is exploratory; see text for limitations.

3.7 Decoherence Length: A Model-Dependent Upper Bound

The decoherence length L_d is estimated from a Lindblad-type open-system model,

$$\frac{d\rho}{dt} = -\frac{i}{\hbar}[H, \rho] + \sum_n \left(L_n \rho L_n^\dagger - \frac{1}{2}\{L_n^\dagger L_n, \rho\} \right), \tag{21}$$

with collapse operators $L_n = \sqrt{\Gamma}\,|d\rangle\langle np|$ that model the coupling to an unspecified environment. This is a toy model whose only purpose is to provide an order-of-magnitude estimate; a realistic treatment would require a model of the nuclear medium and of its coupling to the np pair. Solving Eq. (21) for the spatial coherence gives

$$L_d = \frac{\hbar v_{\rm rel}}{\Gamma}, \tag{22}$$

where $v_{\rm rel}$ is the relative np velocity and Γ the decoherence rate. For thermal neutrons $v_{\rm rel} \approx 2 \times 10^3$ m/s. With a radiative-capture width of order $\Gamma \approx 10^{-3}$ eV, Eq. (22) gives

$$L_d \approx \frac{(1.055 \times 10^{-34}\,\mathrm{J\cdot s})(2 \times 10^3\,\mathrm{m/s})}{(10^{-3})(1.602 \times 10^{-19}\,\mathrm{J})} \approx 1.3 \times 10^{-9}\,\mathrm{m}, \tag{23}$$

which is far larger than any nuclear scale (fm) but far smaller than the 10^{-4} m that would be obtained by using a much smaller Γ. The difference between the two estimates

is a useful reminder that L_d is extremely sensitive to the assumed decoherence rate. The value in Eq. (23) should be interpreted as an upper bound obtained by identifying the decoherence rate with the radiative width, which is the smallest relevant rate; the true decoherence rate in a nuclear environment is dominated by the strong interaction and is many orders of magnitude larger, so that the true L_d is correspondingly smaller. The estimate therefore does not by itself imply long-range quantum correlations in the nuclear sense.

The physical interpretation of this result deserves a comment. A large upper bound on the decoherence length means that the spatial coherence of the np system is not destroyed by the radiative capture itself, which is not surprising given how weak the electromagnetic coupling is at thermal energies. What the estimate does not show is that the coherence survives the strong-interaction environment, which is the more relevant question for any claim about long-range entanglement. A proper treatment of the latter would require a model of the nuclear medium and of its coupling to the np pair, and that is beyond the scope of the present work.

4 Summary and Conclusions

We have built a theoretical framework for entanglement witnesses in the neutron–proton system and applied it to scattering and to radiative capture. The witness operator of Eq. (10) acts on the physical $\mathcal{H}_d \otimes \mathcal{H}_\gamma$ space; its Hermiticity has been shown, and the separability bound has been enforced through the explicit rescaling factor c_W of Eq. (13), with the result verified both analytically and numerically using separable and entangled test states. Within the present two-nucleon model the rescaled witness takes a negative expectation value at low energy, $\langle \tilde{W} \rangle = -0.42 \pm 0.02$ at thermal energy, which signals d–γ entanglement in the final state and, through the coherent electromagnetic transition, points to non-classical correlations generated in the np system. The negativity of $\rho_{d\gamma}$ provides an independent confirmation of the entanglement interpretation. The response of the witness to variations of the tensor force, measured through the dimensionless logarithmic metric of Eq. (16), is larger than that of the quadrupole moment by a factor of about 3.2; the dimensionless nature of the metric is what makes the comparison meaningful. The $np \to d\gamma$ cross section calculated with AV18 agrees with experiment at the few-percent level, with the best agreement (0.03%) at thermal energy. The connection between the witness and the astrophysical S-factor of $d(p,\gamma)^3$He remains exploratory: the enhancement obtained from the parametrization of Eq. (20) is an illustration of the sensitivity to the witness, not a first-principles three-body result, and a full three-body calculation together with a dedicated BBN analysis would be needed before any cosmological claim could be sustained. The decoherence-length estimate $L_d \sim 10^{-9}$ m (Eq. (23)) is an upper bound that reflects the small radiative width rather than long-range nuclear entanglement. The present work is restricted to the two-nucleon system. The extension to three-nucleon systems, the experimental implementation of the witness and the BBN analysis are left for future work, and all quantitative statements in this paper should be read within these limitations.

Statements and declarations

- **Author contribution**: H. Sadeghi and M. Mirzaee devised the conceptual framework. H. Sadeghi compiled the technical details and M. Mirzaee performed the numerical calculations. Both authors contributed to the interpretation of the results and to the writing of the manuscript.
- **Data Availability**: The computational code and the numerical data underlying Tables 1–7 are available from the corresponding author on reasonable request and will be deposited in a public repository upon publication.
- **Conflict of Interest**: The authors declare no conflict of interest.
- **Funding**: No funding was received for this work.

References

[1] R. Horodecki, P. Horodecki, M. Horodecki, and K. Horodecki, *Quantum entanglement*, Rev. Mod. Phys. **81**, 865–942 (2009).

[2] C. Dumbrajs, R. Koch, H. Pilkuhn, G. C. Oades, H. Behrens, J. J. de Swart, and P. Kroll, *Solution of the nucleon-nucleon scattering problem*, Nucl. Phys. B **216**, 277–298 (1983).

[3] H. Yukawa, *On the interaction of elementary particles*, Proc. Phys. Math. Soc. Japan **17**, 48–57 (1935).

[4] E. Epelbaum, H.-W. Hammer, and U.-G. Meißner, *Modern theory of nuclear forces*, Rev. Mod. Phys. **81**, 1773–1825 (2009).

[5] R. Machleidt, *The high-precision, charge-dependent Bonn nucleon-nucleon potential*, Phys. Rev. C **63**, 024001 (2001).

[6] A. K. Ekert, C. M. Alves, D. K. L. Oi, *et al.*, *Direct estimations of linear and nonlinear functionals of a quantum state*, Phys. Rev. Lett. **88**, 217901 (2002).

[7] M. A. Nielsen and I. L. Chuang, *Quantum Computation and Quantum Information*, Cambridge University Press (2010).

[8] M. Mirzaee and H. Sadeghi, *Quantum coherence in radiative capture reactions*, Sci. Rep. **15**, 16401 (2025).

[9] R. B. Wiringa, V. G. J. Stoks, and R. Schiavilla, *Accurate nucleon-nucleon potential with charge-independence breaking*, Phys. Rev. C **51**, 38–51 (1995).

[10] V. G. J. Stoks, R. A. M. Klomp, C. P. F. Terheggen, and J. J. de Swart, *Construction of high-quality NN potential models*, Phys. Rev. C **49**, 2950 (1994).

[11] H. Lehmann, K. Symanzik, and W. Zimmermann, *Zur Formulierung quantisierter Feldtheorien*, Nuovo Cimento **1**, 205–225 (1955).

[12] M. E. Peskin and D. V. Schroeder, *An Introduction to Quantum Field Theory*, Westview Press (1995), Ch. 4.

[13] J. C. Ward, *An identity in quantum electrodynamics*, Phys. Rev. **78**, 182 (1950).

[14] P. Lepage, *How to renormalize the Schrödinger equation*, arXiv:nucl-th/9706029 (1997).

[15] E. Hairer, S. P. Nørsett, and G. Wanner, *Solving Ordinary Differential Equations I*, 2nd ed., Springer (1993), Ch. II.

[16] R. Schiavilla, V. R. Pandharipande, and D. O. Riska, *Magnetic form factors of the deuteron*, Phys. Rev. C **41**, 309 (1990).

[17] S. Pastore *et al.*, *Electromagnetic two-body currents of one- and two-pion range*, Phys. Rev. C **78**, 064002 (2008).

[18] L. L. Foldy and S. A. Wouthuysen, *On the Dirac theory of spin 1/2 particles and its non-relativistic limit*, Phys. Rev. **78**, 29–36 (1950).

[19] V. Huhn *et al.*, *Measurement of the spin transfer coefficients for the* $^1H(\vec{n},\vec{d})\gamma$ *reaction at thermal neutron energies*, Phys. Rev. Lett. **85**, 1190 (2000).

[20] G. Vidal and R. F. Werner, *Computable measure of entanglement*, Phys. Rev. A **65**, 032314 (2002).

[21] L. E. Marcucci *et al.*, *Proton-deuteron radiative capture cross section below the deuteron breakup*, Phys. Rev. C **93**, 024003 (2016).

[22] R. Schiavilla *et al.*, *Electromagnetic structure of the deuteron*, Phys. Rev. C **58**, 1263 (1998).

[23] Y. Nagai *et al.*, *Experimental study of the* $np \to d\gamma$ *reaction cross section*, Phys. Rev. C **77**, 034601 (2008).

[24] LUNA Collaboration, C. Casella *et al.*, *First measurement of the* $d(p,\gamma)^3He$ *cross-section down to the solar Gamow peak*, Nucl. Phys. A **706**, 203 (2002).